npj computational materials

www.nature.com/npjcompumats

ARTICLE OPEN

Long-range current-induced spin accumulation in chiral crystals

Arunesh Roy[1], Frank T. Cerasoli[2,5], Anooja Jayaraj[2,5], Karma Tenzin[1,3,5], Marco Buongiorno Nardelli[2,4] and Jagoda Sławińska[1]✉

Chiral materials, similarly to human hands, have distinguishable right-handed and left-handed enantiomers which may behave differently in response to external stimuli. Here, we use for the first time an approach based on the density functional theory (DFT) +PAOFLOW calculations to quantitatively estimate the so-called collinear Rashba–Edelstein effect (REE) that generates spin accumulation parallel to charge current and can manifest as chirality-dependent charge-to-spin conversion in chiral crystals. Importantly, we reveal that the spin accumulation induced in the bulk by an electric current is intrinsically protected by the quasi-persistent spin helix arising from the crystal symmetries present in chiral systems with the Weyl spin–orbit coupling. In contrast to conventional REE, spin transport can be preserved over large distances, in agreement with the recent observations for some chiral materials. This allows, for example, the generation of spin currents from spin accumulation, opening novel routes for the design of solid-state spintronics devices.

npj Computational Materials (2022)8:243 ; https://doi.org/10.1038/s41524-022-00931-3

INTRODUCTION

Several phenomena in nature are governed by the geometric property called chirality. Chiral molecules and crystals have a property of handedness arising from the lack of inversion, mirror, and roto-inversion symmetries, and host a plethora of intriguing effects manifesting differently in opposite enantiomers[1–4]. Among these phenomena, the chirality-induced spin selectivity (CISS) describing the generation of a collinear spin current by a charge current flowing through a chiral molecule or assembly, is one of the most intriguing[5,6]. A similar effect was recently realized in solid-state materials with strong spin–orbit coupling (SOC), opening a perspective for the design of devices based on the robust properties protected by crystal symmetries[7–12]. The observation of the chirality-dependent charge-to-spin conversion (CSC) was assigned to the collinear Rashba–Edelstein effect (REE) using the symmetry analysis and models. However, a reliable quantitative description of spin accumulation induced by electric currents in chiral materials is still lacking.

Here, we develop and implement a computational approach to calculate current-induced spin accumulation in periodic systems based on density functional theory (DFT) and tight-binding Hamiltonians generated in the PAOFLOW code[13,14]. We further perform calculations of the magnetization induced by electric currents in Te and $TaSi_2$, two different chiral materials with strong spin–orbit coupling (SOC), and compare them with experiments. Since the spin accumulation parallel to a charge current arises from the radial spin texture determined by the chiral point group symmetry, we analyze the landscape and symmetry of the spin–orbit field to explain in detail the properties of spin transport in chiral crystals. In particular, we demonstrate that the Weyl-type SOC term locally describing the radial spin texture, may generate a quasi-persistent spin helix in the real space which prevents the spin randomization and results in a very long spin lifetime in a diffusive transport regime. The collinear spin accumulation induced in chiral materials, in contrast to the conventional REE, is thus intrinsically protected from the spin decoherence which may have a far-reaching impact on the design of spintronics devices.

RESULTS AND DISCUSSION

Calculation of the current-induced spin accumulation for arbitrary SOC

The spin accumulation also referred to as current-induced spin polarization (CISP), is a non-equilibrium magnetization induced by an electric current that flows through a non-magnetic material with a large SOC[15–18]. Even though it was discovered decades ago, experimental studies typically addressed its special case, the Rashba–Edelstein effect present in systems with the Rashba-type spin-momentum locking, such as a two-dimensional electron gas (2DEG), interfaces and surfaces with broken inversion symmetry[19–21]. The fact that the spin accumulation might arise from any other type of SOC, such as Dresselhaus, Weyl, or more complex spin arrangements, was often disregarded and alternative configurations were less studied, being mostly limited to models[22].

We will start with a brief overview of the implemented computational approach that allows the calculation of the spin accumulation for arbitrary SOC. The equilibrium electron distribution in a crystal can be described by the Fermi distribution function $f^0_{\mathbf{k}}$. Due to the time-reversal symmetry, the expectation values of the spin operator $\mathbf{S}$ at the opposite momenta cancel, resulting in a zero net spin polarization. Upon the flow of charge current, the spin-polarized Fermi surface shifts as a result of the applied field and the non-equilibrium distribution $f_{\mathbf{k}} = f^0_{\mathbf{k}} + \delta f_{\mathbf{k}}$ generates a net spin polarization:

$$\delta \mathbf{s} = \sum_{\mathbf{k}} \langle \mathbf{S} \rangle_{\mathbf{k}} \delta f_{\mathbf{k}} \tag{1}$$

[1]Zernike Institute for Advanced Materials, University of Groningen, Nijenborgh 4, 9747AG Groningen, The Netherlands. [2]Department of Physics, University of North Texas, Denton, TX 76203, USA. [3]Department of Physical Science, Sherubtse College, Royal University of Bhutan, 42007Kanglung, Trashigang, Bhutan. [4]The Santa Fe Institute, Santa Fe, NM 87501, USA. [5]These authors contributed equally: Frank T. Cerasoli, Anooja Jayaraj, Karma Tenzin. ✉email: jagoda.slawinska@rug.nl

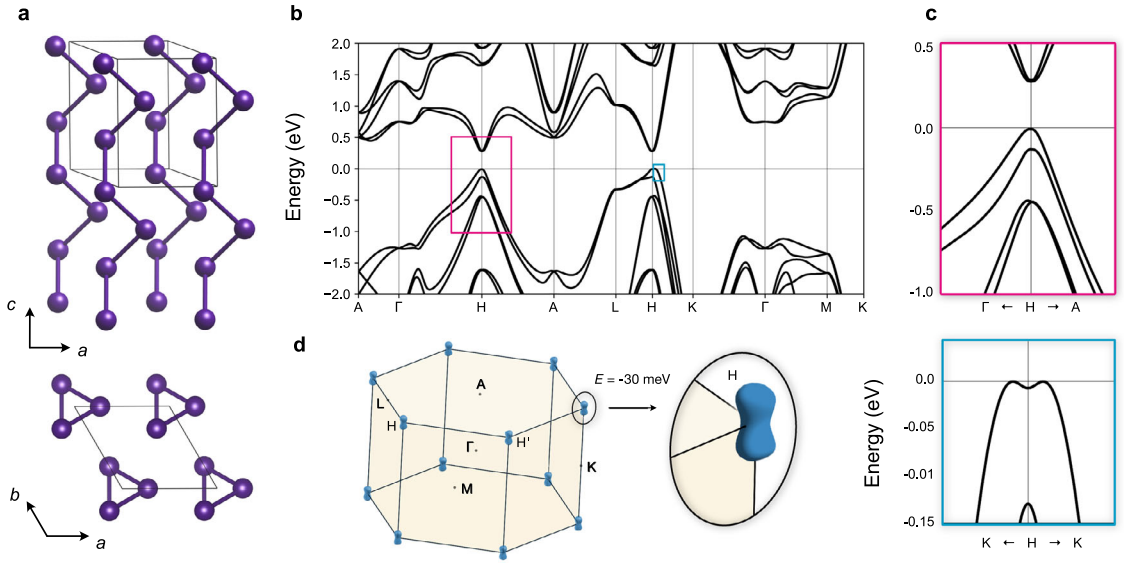

Fig. 1 Crystal structure and electronic properties of chiral tellurium. a Side and top view of the left-handed Te (SG 154). **b** Band structure calculated along the high-symmetry lines in the Brillouin zone (BZ), identical for both enantiomers. **c** Zoom on the two regions marked by the color rectangles in (**b**). The upper panel shows the set of 5*p* lone-pair bands around the H point. The bottom panel illustrates the details of the topmost valence band. **d** Brillouin zone with the high-symmetry points and Fermi surface at $E = -30$ meV; the inset shows a zoom-in of the dumbbell-shaped hole pocket at the H point.

We can calculate $\delta f_{\mathbf{k}}$ in the framework of the semi-classical Boltzmann transport theory and write:

$$\delta \mathbf{s} = \sum_{\mathbf{k}} \langle \mathbf{S} \rangle_{\mathbf{k}} \tau_{\mathbf{k}} (\mathbf{v}_{\mathbf{k}} \cdot \mathbf{E}) \frac{\partial f_{\mathbf{k}}}{\partial E_{\mathbf{k}}} \tag{2}$$

where $\tau_{\mathbf{k}}$ is the relaxation time and $\mathbf{v}_{\mathbf{k}}$ the group velocity. Because the charge current density can be expressed using the same $\delta f_{\mathbf{k}}$[23]

$$\mathbf{j_c} = -\frac{e}{V} \sum_{\mathbf{k}} \mathbf{v}_{\mathbf{k}} \delta f_{\mathbf{k}}. \tag{3}$$

we can introduce the spin accumulation tensor χ defined as the ratio of the quantities from Eqs. (2) and (3),

$$\chi^{ji} = -\frac{\sum_{\mathbf{k}} \langle \mathbf{S} \rangle^j_{\mathbf{k}} \mathbf{v}^i_{\mathbf{k}} \frac{\partial f_{\mathbf{k}}}{\partial E_{\mathbf{k}}}}{e \sum_{\mathbf{k}} (\mathbf{v}^i_{\mathbf{k}})^2 \frac{\partial f_{\mathbf{k}}}{\partial E_{\mathbf{k}}}} \tag{4}$$

in which we assumed the constant relaxation time approximation. The induced spin accumulation per unit volume can be then calculated from the formula:

$$\delta s^j = \chi^{ji} j_i^{\mathrm{A}} \tag{5}$$

where j_i^{A} is the value of the charge current applied along an arbitrary i direction. Consequently, we can calculate the induced magnetization per unit cell as

$$\mathbf{m} = -g_s \mu_{\mathrm{B}} V \delta \mathbf{s} / \hbar \tag{6}$$

where $g_s = 2$ is the Landé g-factor, μ_{B} is Bohr magneton and V denotes the volume of the unit cell.

The quantities required to compute the tensor χ for any material can be evaluated using accurate ab initio tight-binding (TB) Hamiltonians constructed from self-consistent quantum-mechanical wavefunctions projected onto a set of atomic orbitals, as detailed in the "Methods" section[24]. Alternative approaches for the calculations of spin accumulation can be found in the previous studies[25,26].

Unconventional charge-to-spin conversion in Te

One of the simplest chiral crystals is trigonal tellurium that crystallizes in two enantiomorphic structures sharing the point group D_3, the right-handed described by the space group $P3_121$ (SG 152) and the left-handed belonging to the space group $P3_221$ (SG 154); the structure of the latter is schematically shown in Fig. 1a. Te atoms form covalently bonded spiral chains which are arranged hexagonally and interact with each other via weak van der Waals forces. The threefold screw symmetry C_3 that determines the chirality runs along the *c*-axis, while the additional twofold rotational symmetry axes C_2 lie within the $a-b$ plane. The calculated electronic structure is presented in Fig. 1b, c and agrees well with the earlier theoretical and experimental findings[27–32]. While it is difficult to reproduce the semiconducting behavior of Te by standard simulations based on the generalized-gradient or local-density approximation, the calculations within the novel pseudo-functional approach ACBN0 yield a gap of 279 meV which is close to the measured value of 330 meV[33], and capture the characteristic 'camelback' shape of the topmost valence band (VB) with a local maximum along the H-K line[34].

The strong spin–orbit interaction in Te combined with the lack of the inversion symmetry results in a large spin-splitting of the bands in the whole energy range, but only the topmost VB contributes to electronic and spin transport. Due to the intrinsic p-type doping coming from the vacancies, the Fermi level is shifted by a few tens meV below the VBM and the Fermi surface consists of two small pockets around the H and H' points (Fig. 1d), with size and shape depending on the doping. The constant energy contours shown in Fig. 2a correspond to pockets of different sizes projected onto the k_x-k_z plane passing through the H point, while the superimposed color maps represent S_x, S_y, and S_z components of the spin texture.

The peculiar orientation of spins, radial toward the H and H' points are enforced by the three-fold screw symmetry along the K–H line and the twofold symmetry with respect to the H–H' lines in the absence of any mirror planes[7,31]. Such a spin arrangement, resembling a magnetic monopole in the reciprocal space, is a signature of the prototypical Weyl-type SOC and may occur only in the systems lacking mirror symmetry. Moreover, the S_z component prevailing over S_x and S_y, indicates that the spin texture is almost entirely aligned with the k_z, and suggests its quasi-persistent character. The radial spin texture of trigonal Te, including spin polarization nearly parallel to the long direction of the hole

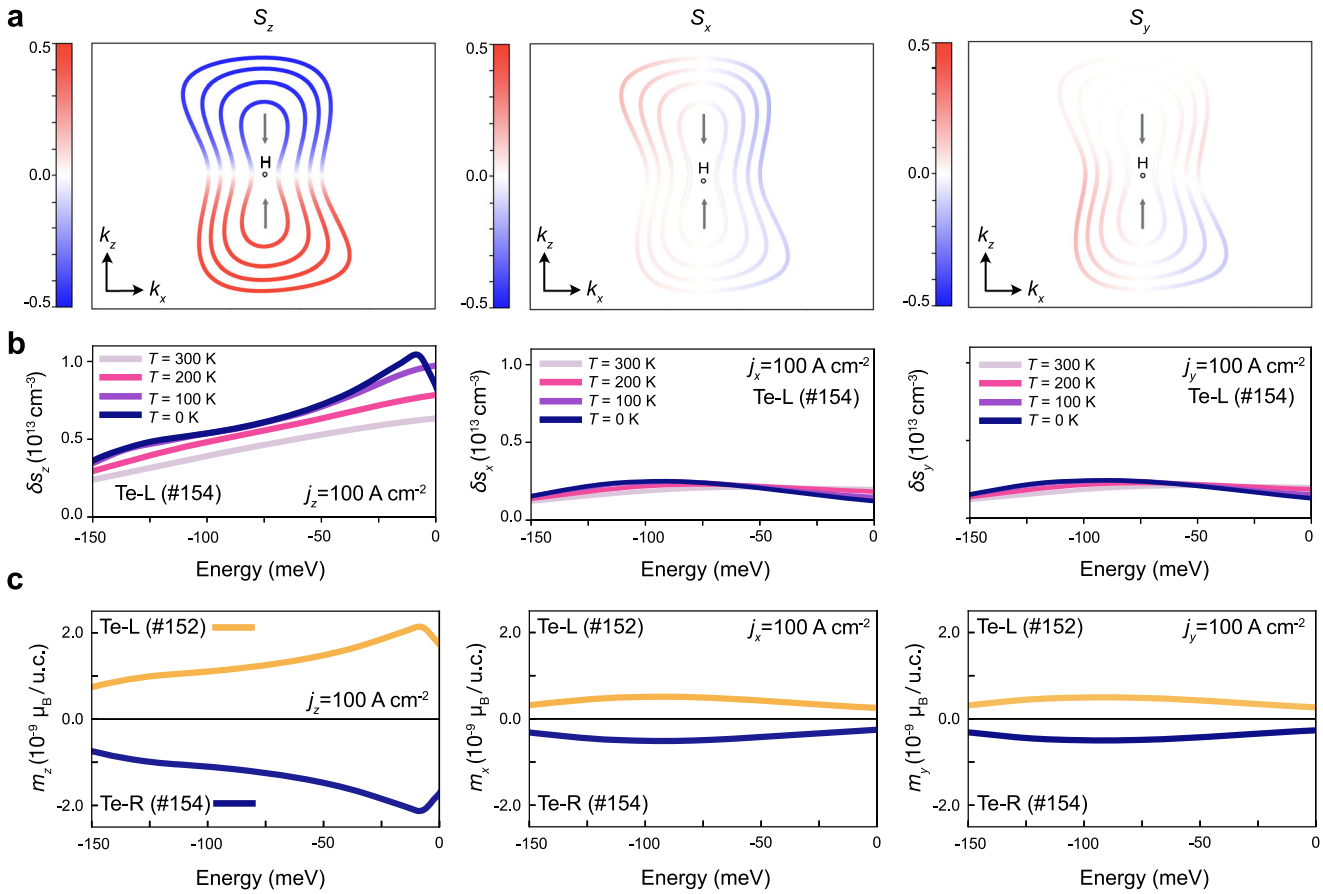

Fig. 2 Spin-resolved electronic structure and spin accumulation in bulk Te. a The calculated isoenergy contours projected onto the k_x–k_z plane passing through the H point in the left-handed Te. The energy eigenvalues are selected at 10, 30, 50, and 70 meV below the Fermi level, counting from the center. The color maps superimposed on the contours represent the expectation values of S_x, S_y, and S_z shown at the left, middle, and right panels, respectively. The spin texture is radial with respect to the H point and nearly persistent along k_z, as indicated by the arrows. **b** Spin accumulation per volume induced by the charge current $j = 100$ A cm^2 applied along z, x, and y direction in the left-handed Te, represented by left, middle, and right panel, respectively. Different lines correspond to temperatures in the range from 0 to 300 K. **c** The corresponding magnetization per unit cell was calculated for the left-handed (blue lines) and right-handed Te (orange lines) at 0 K.

pocket, was confirmed by the recent spin- and angle-resolved photoemission spectroscopy (S-ARPES) measurements[35,36].

Based on the accurate spin-resolved electronic structure, we calculated the chirality-dependent spin accumulation induced by an applied electric current. Because the spins around the H and H′ points are parallel to the momentum, any projection of $\delta\mathbf{s}$ can be achieved as long as the charge current flows in the same direction. This is in line with the symmetry analysis that we performed in the spirit of Seemann et al.[37–39], revealing that the χ tensor will indeed contain only diagonal elements. The components δs_z, δs_x, and δs_y induced by the electric current of 100 A cm^{-2} along the z, x, and y directions, respectively, are plotted in the left, middle, and right panel of Fig. 2b. Although the spin accumulation perpendicular to the screw axis was never reported for chiral Te, it is evident that the components δs_x and δs_y, albeit lower than δs_z by an order of magnitude, are present and could be observed in experiments.

The dependence of δs_z on chemical potential (Fig. 2b), closely reflects the electronic structure and the spin texture of the topmost VB. The highest (negative) value of the spin accumulation coincides with the local band minimum at the H point (−8 meV, the bottom panel in Fig. 1c), and it decreases when approaching the next valence band with the opposite spin polarization. Although reaching its edge at −130 meV with respect to E_F would require unrealistic values of doping (approximately 2.3×10^{19} vs. 10^{14}–10^{17} cm^{-3} typically observed in Te samples[40,41]), the decrease in the magnitude can be noticed already above this value. Thus, the low concentrations of holes seem to maximize the spin accumulation in Te. Another factor that may play a relevant role is the temperature (see Fig. 2b). In particular, δs_z tends to drop by a factor of two at room temperature, which cannot be easily explained and requires further systematic studies. In contrast, the components δs_x and δs_y do not strongly depend either on doping or on temperature.

Finally, we will compare the current-induced magnetization calculated from Eq. (6) and displayed in Fig. 2c with the values obtained based on the nuclear magnetic resonance measurements.[7] Our predicted magnetization of $10^{-9}\mu_B$ per unit cell agrees well with the model conceived by Furukawa et al.[7], but it is one order of magnitude lower than the value estimated from their experimental data ($10^{-8}\mu_B$). In addition, our calculated dependence of the induced spin accumulation on chemical potential agrees very well with the experimental trend revealed recently for Te nanowires[9]. Importantly, the collinear REE being directly linked to the spin texture, yields exactly opposite signs of $\delta\mathbf{m}$ for different enantiomers which are connected by the inversion symmetry operation (see Fig. 2c), in line with the observed chirality-dependent charge-to-spin conversion.

CISP in a semimetallic disilicide $TaSi_2$

Inspired by the spin transport experiments that revealed signatures of chirality-dependent response in disilicides, we performed the calculations for chiral $TaSi_2$ [12]. Its right-handed

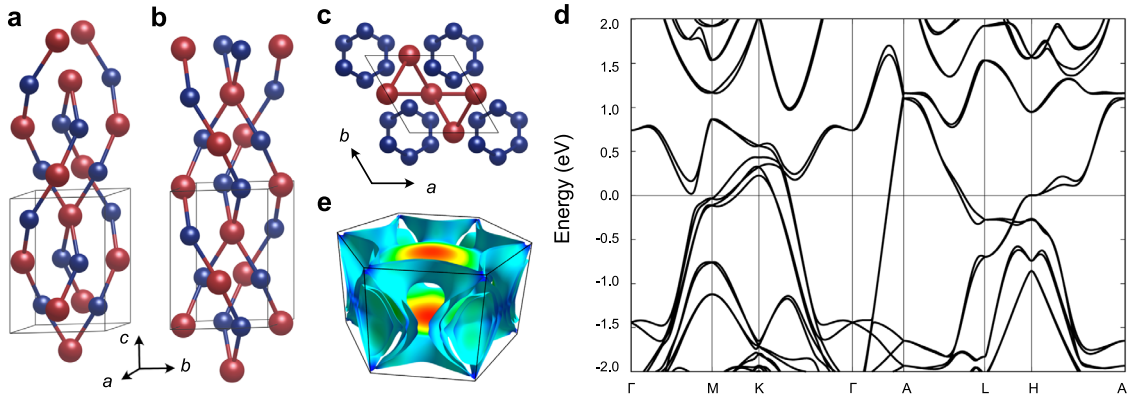

Fig. 3 Structure and electronic properties of chiral $TaSi_2$. a Side view of the right-handed $TaSi_2$ (SG 180). Ta atoms are denoted as red and Si atoms as blue balls. **b** Top and side view of the left-handed $TaSi_2$ (SG 181). **c** The calculated Fermi surface ($E = E_F$) consists of four nested sheets. The color scheme reflects the Fermi velocity[57]. **d** Band structure calculated along the high-symmetry lines in the momentum space. The high-symmetry points are consistent with the labels in Fig. 1.

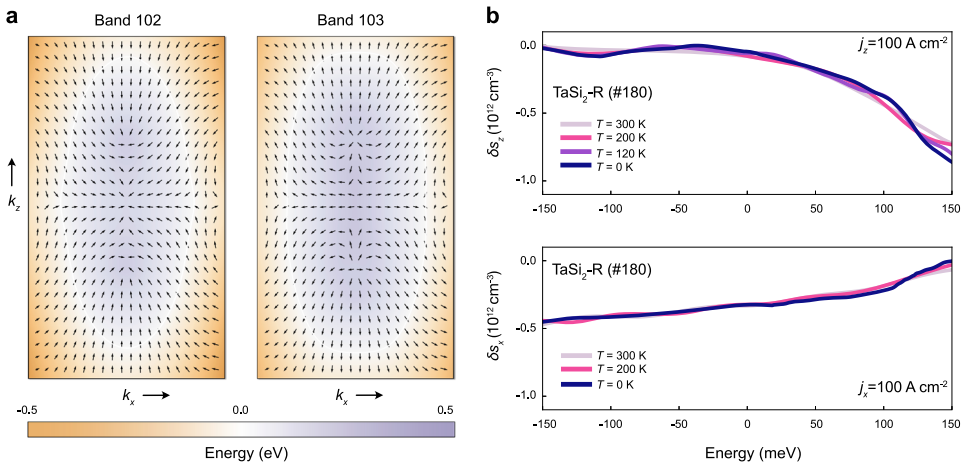

Fig. 4 Spin texture and spin accumulation in the right-handed $TaSi_2$ (SG 180). a Energy eigenvalues and spin texture of the two innermost bands visible in Fig. 3e projected on the k_x–k_z plane passing through the K point; the K point is located exactly at the center. The S_y components are included only in the norms of the spin vectors. The multiple arrows serve as a better illustration of the trend, but only those coinciding with the Fermi contour—denoted as the white line—contribute to the spin accumulation. **b** The calculated spin accumulation vs energy; the components δs_z and δs_x are shown in the upper and bottom panels, respectively. The omitted δs_y is similar to δs_x. The colors of the lines correspond to different temperatures.

structure belongs to the space group $P6_222$ (SG 180), and the left-handed one is characterized by the space group $P6_422$ (SG 181); both enantiomers are displayed in Fig. 3a, b. The hexagonal unit cell contains two pairs of intertwined Ta–Si–Ta chains with different helicity running along the c direction, which is reversed for the opposite enantiomers. The left-handed and right-handed structures are distinguished by the sixfold screw symmetry C_6 along the c-axis, while the additional C_2 rotational symmetries are defined with respect to the crystal a–b face diagonals (see Fig. 3c). The calculated electronic structure shown in Fig. 3d is in a good agreement with the existing theoretical and experimental reports[42–44]. $TaSi_2$ is a Weyl semimetal and indeed, the energy dispersion contains several degenerate crossings protected by the nonsymmorphic symmetry, for example, the nodes at the M and H points that lie close to the Fermi level. The shape of the Fermi surface (Fig. 3e), consisting of four non-intersecting sheets is also in line with the results of the previous de Haas–van Alphen experiments[42].

The current-induced spin accumulation in the semimetallic $TaSi_2$ is governed by the spin texture of the Fermi surface. Because it contains multiple nested sheets with different spin patterns, it is not straightforward to analyze the full landscape of the spin–orbit field inside the BZ. Nevertheless, the linear-in-k spin arrangement at the high-symmetry points can be predicted with the help of the group theory and further verified by the DFT calculations. Following the study by Mera Acosta et al.[45], we note that the crystallographic point group D_6 describing $TaSi_2$ may yield the purely radial Weyl spin texture at the k-vectors possessing the point group symmetry D_3 or D_6. Using the Bilbao Crystallographic Server[46,47], we determined little point groups of all the high-symmetry points (Γ, A, K, H, and M) and we found that most of them can be the 'source' or 'sink' of the radial spin texture. Only the M point described by the little point group D_2 allows both Weyl and Dresselhaus spin arrangement[45]. As an example, Fig. 4a illustrates the spin texture of the two innermost bands contributing to the Fermi surface, projected onto the k_x–k_z plane around the K point. The spin textures are almost perfectly radial with a visible persistent component S_z that seems to be enforced by the elongated band shapes. In a 3D k-space, these FS would resemble ellipsoids, one inside another, with hedgehog-like spin textures.

The radial spin arrangements dominating the BZ, generate the unconventional spin accumulation that may manifest as the spin selectivity in $TaSi_2$. The calculated $\delta\mathbf{s}$ induced by the electric current of 100 A cm^{-2} flowing in the directions parallel and perpendicular to the screw axis is shown in Fig. 4b. The results are presented as the energy dependence to better show the

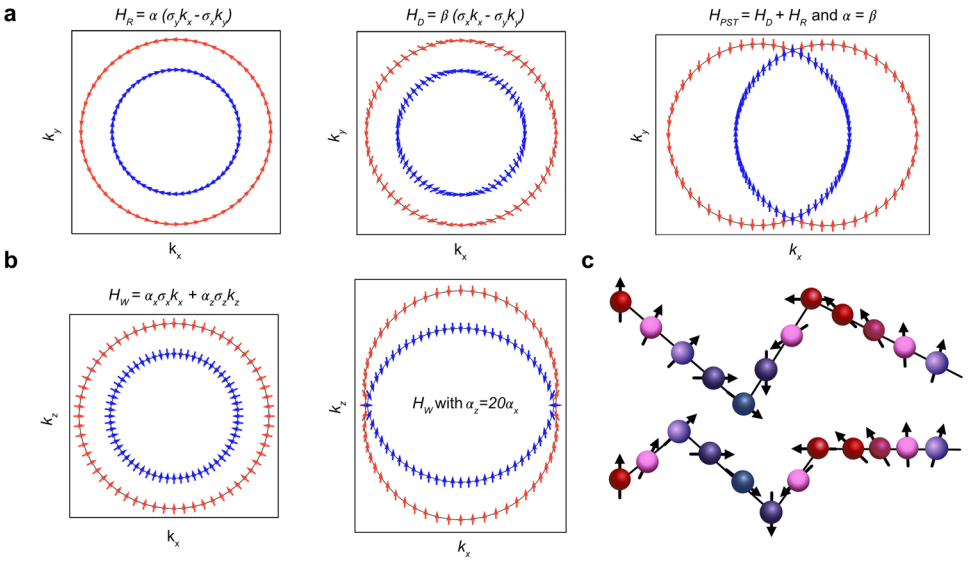

Fig. 5 Persistent spin texture and spin helix in the Rashba–Dresselhaus (RD) and Weyl (W) models enhancing spin transport in systems with strong SOC. a Pure Rashba (left) and Dresselhaus (middle) models; their combination with $\alpha = \beta$ (right) generates a persistent spin texture in the momentum space. **b** Analogous mechanism contributing to a persistent spin texture in the Weyl model describing the radial spin texture; Weyl Hamiltonian with equal ($\alpha_z = \alpha_x$) parameters (left) and with the prevailing $\alpha_z\sigma_z$ term (right). The latter, with $\alpha_z = 20\alpha_x$ closely resembles the spin texture of Te (see Fig. 2a). **c** Schematic illustration of a persistent spin helix in the real space observed in quantum wells with balanced Rashba and Dresselhaus terms[58]. The collective spin is a conserved quantity due to the emergence of the *SU*(2) symmetry. The quasi-persistent spin texture described by the Weyl Hamiltonian will lead to a similar effect protecting the spin transport.

connection with the band structure, but $TaSi_2$ is semimetallic and mostly the values close to the Fermi level are relevant for the transport. Surprisingly, δs_z at E_F is nearly two orders of magnitude lower than in the slightly doped Te (10^{11} vs. 10^{13} cm^{-3}), while δs_x is lower by one order of magnitude. Such a difference seems to be due to the fact that two pairs of bands with opposite polarization simultaneously cross the Fermi level. This contrasts with the case of Te which FS consists of two identical spin-polarized pockets. In fact, the increase of the δs_z magnitude above E_F in $TaSi_2$ can be assigned to the emergence of an isolated strongly spin-polarized pocket at +20 meV.

Chirality-dependent response in disilicides was suggested based on the spin transport experiments for left- and right-handed $NbSi_2$ and $TaSi_2$[12]. Although these reports were quantitative and cannot be compared with the result of the DFT calculations, we believe that the current-induced spin accumulation may give rise to the observed interconversion between charge and spin current. First, we note that the unconventional SHE in $TaSi_2$ (SG 180) is forbidden by symmetry and could not contribute to the collinear spin transport[39]. Second, the quasi-persistent character of the spin texture enforced by the crystal symmetry (Fig. 4a) indicates that the spins accumulated in the bulk should be partially protected from scattering, and capable to diffuse to the detection electrode. Below, we will explicitly show that the anti-symmetric SOC arising from the monoaxial screw symmetry, and approximated by the linear-in-*k* Weyl term in the Hamiltonian[45,48], generates the *near persistent spin helix* in the real space and gives rise to a potentially infinite spin lifetime in chiral materials.

Protection of spin transport over macroscopic distances

To complete the description of spin transport in chiral materials, we will demonstrate the emergence of the *persistent spin helix* that protects from dephasing the spin accumulation generated in the bulk. Let us consider the free electron dispersion $H_0 = \hbar^2 k^2/2m$ where m is the effective electron mass and $\mathbf{k} = (k_x, k_y, k_z)$ and the Weyl spin–orbit coupling term $H_{so} = \alpha_x k_x \hat{\sigma}_x + \alpha_y k_y \hat{\sigma}_y + \alpha_z k_z \hat{\sigma}_z$, where $\hat{\sigma}_i$ denotes the Pauli spin matrices and α_i are the SOC parameters along $i = x, y, z$ directions. Our first-principles calculations show that the spin textures of Te and $TaSi_2$ are strongly enhanced along the direction of the screw axis, as illustrated in Figs. 2a and 4a. More specifically, in the case of Te the SOC parameters are $\alpha_z >> \alpha_j$ for $j = x, y$, whereas in $TaSi_2$ we have $\alpha_z > \alpha_x > \alpha_y$. The Hamiltonian is then, without the loss of generality

$$H = H_0 + H_{so} \simeq \frac{\hbar^2 k_\parallel^2}{2m} + \frac{\hbar^2 k_z^2}{2m} + \alpha_z k_z \hat{\sigma}_z, \tag{7}$$

where $k_\parallel^2 = k_x^2 + k_y^2$. The Hamiltonian is diagonal in the spin space and its eigenvalues are

$$E_{\uparrow,\downarrow}(\mathbf{k}) = \frac{\hbar^2 k_\parallel^2}{2m} + \frac{\hbar^2}{2m}\left(k_z \mp \frac{m\alpha_z}{\hbar^2}\right)^2 - \frac{\hbar^2}{2m}\left(\frac{m\alpha_z}{\hbar^2}\right)^2, \tag{8}$$

where $E_{\uparrow,\downarrow}$ denote bands with ↑,↓ spin projections, respectively. Eq. (8) satisfies the shifting property

$$E_\uparrow(\mathbf{k}) = E_\downarrow(\mathbf{k} + \mathbf{Q}), \tag{9}$$

proposed by Berenevig et al., which implies that the Fermi surfaces consist of two circles, shifted by magic-shifting vector $\mathbf{Q} = 2m\alpha_z/\hbar^2$ [49]. Following the analysis similar to the one for the Rashba–Dresselhaus model with equal SOC parameters[49], we identify the existence of the *SU*(2) symmetry of the Hamiltonian in Eq. (7), which is robust against disorder and Coulomb interaction and can give rise to, ideally, infinite spin lifetime along the *z*-direction (see Fig. 5). The presence of the weak SOC along the *x* and *y* directions, perturbs the exact *SU*(2) symmetry. The *near persistent spin helix* yields the finite, but sizable spin relaxation length and makes possible the detection of the spin accumulation induced by the electric current in the bulk chiral crystals[10,12].

In summary, we calculated the collinear Rashba–Edelstein effect originating from radial spin textures, using for the first time the accurate DFT-based approach that allowed us to estimate the induced magnetic moment per unit cell for two representative chiral materials Te and $TaSi_2$. While the values and dependence on chemical potential calculated for the former are in agreement with the recent experiments, confirming that the observed chirality-dependent charge-to-spin conversion indeed originates from spin

accumulation[7,9], our approach implemented in PAOFLOW will allow for further calculations of spin transport in materials studied experimentally. Importantly, we also proved via the analysis of the calculated spin textures and a general Weyl Hamiltonian, that the chiral materials can host the quasi-persistent spin helix emerging in the real space as a consequence of the crystal symmetry. It protects spins against scattering and ensures a sizable spin relaxation length, which seems to be in line with the recent observation of micrometer-range spin transport. This makes the collinear REE different from the conventional one, where the bulk spin accumulation gets easily randomized. The possibility of electric generation of spin accumulation, preserving at the same time the long spin lifetime, will have important implications for spintronics devices.

METHODS

First-principles calculations

We performed calculations based on the density functional theory (DFT) using the QUANTUM ESPRESSO package[50,51]. We treated the ion–electron interaction with the fully relativistic pseudopotentials from the pslibrary (0.2) database[52], and expanded the electron wave functions in a plane wave basis set with the cutoff of 80 Ry. The exchange and correlation interaction was taken into account within the generalized gradient approximation (GGA) parameterized by the Perdew, Burke, and Ernzerhof (PBE) functional[53]. The Te crystals were modeled using hexagonal unit cells containing three atoms, which were fully optimized with the convergence criteria for energy and forces set to 10^{-5} Ry and 10^{-4} Ry/Bohr, respectively. We applied the Hubbard correction calculated self-consistently using the ACBN0 method[54], which value $U_{5p} = 3.81$ eV was included in the relaxations and the electronic structure calculations. The lattice constants were optimized to $a = b = 4.51$ Å and $c = 5.86$ Å. $TaSi_2$ was modeled in a hexagonal unit cell containing nine atoms. The lattice parameters were fixed to the experimental values $a = b = 4.78$ Å and $c = 6.57$ Å[43], while the internal coordinates were relaxed. The BZ integrations were performed using the Monkhorst–Pack scheme with k-points grids of $22 \times 22 \times 16$ and $16 \times 16 \times 12$ for Te and $TaSi_2$, respectively. The Gaussian smearing of 0.001 Ry was chosen as the orbital occupation scheme. SOC was included self-consistently in all the calculations.

Spin transport calculations

Current-induced spin accumulation was evaluated as a post-processing step using the tight-binding (TB) approach implemented in the PAOFLOW code[13,14]. We have started with the ab initio wavefunctions, projecting them onto the pseudoatomic orbitals in order to construct accurate tight-binding (PAO) Hamiltonians[55,56]. We further interpolated these Hamiltonians onto ultra-dense k-points meshes of $140 \times 140 \times 110$ for Te and $80 \times 80 \times 60$ for $TaSi_2$, and we directly evaluated the quantities that are required to compute spin accumulation from Eq.(4). In particular, the group velocities $\mathbf{v_k}$ are calculated as Hamiltonian's gradients $(1/\hbar)dH/d\mathbf{k}$, and the spin polarization of each eigenstate $\psi(\mathbf{k})$ is automatically taken as the expectation value of the spin operator $\langle\psi(\mathbf{k})|\mathbf{S}|\psi(\mathbf{k})\rangle$ [14]. For an arbitrary energy E, the derivative of the Fermi distribution at zero temperature is equal to $\delta(E_\mathbf{k}-E)$ which we approximated with a Gaussian function. For $T > 0$, we explicitly calculated the derivative of the Fermi–Dirac distribution. We note that the adaptive smearing method could not be applied in this case, and a larger k-grid of $140 \times 140 \times 100$ had to be used to converge the calculation of $TaSi_2$ (Fig. 4c). The influence of the temperature on the electronic structures was not taken into account.

DATA AVAILABILITY

Data are available from the authors upon reasonable request.

CODE AVAILABILITY

The PAOFLOW code can be downloaded from http://aflowlib.org/src/paoflow/.

Received: 5 June 2022; Accepted: 2 November 2022;
Published online: 18 November 2022

REFERENCES

1. Hendry, E. et al. Ultrasensitive detection and characterization of biomolecules using superchiral fields. *Nat. Nanotechnol.* **5**, 783–787 (2010).
2. Kelly, C. et al. Controlling the symmetry of inorganic ionic nanofilms with optical chirality. *Nat. Commun.* **11**, 5169 (2020).
3. Hentschel, M., Schäferling, M., Duan, X., Giessen, H. & Liu, N. Chiral plasmonics. *Sci. Adv.* **3**, e1602735 (2017).
4. Ayuso, D. et al. Synthetic chiral light for efficient control of chiral light–matter interaction. *Nat. Photonic* **13**, 866–871 (2019).
5. Evers, F. et al. Theory of chirality induced spin selectivity: Progress and challenges. *Adv. Mater.* **34**, 2106629 (2022).
6. Waldeck, D. H., Naaman, R. & Paltiel, Y. The spin selectivity effect in chiral materials. *APL Mater.* **9**, 040902 (2021).
7. Furukawa, T., Shimokawa, Y., Kobayashi, K. & Itou, T. Observation of current-induced bulk magnetization in elemental tellurium. *Nat. Commun.* **8**, 954 (2017).
8. Furukawa, T., Watanabe, Y., Ogasawara, N., Kobayashi, K. & Itou, T. Current-induced magnetization caused by crystal chirality in nonmagnetic elemental tellurium. *Phys. Rev. Res.* **3**, 023111 (2021).
9. Calavalle, F. et al. Gate-tuneable and chirality-dependent charge-to-spin conversion in tellurium nanowires. *Nat. Mater.* **21**, 526–532 (2022).
10. Inui, A. et al. Chirality-induced spin-polarized state of a chiral crystal $CrNb_3S_6$. *Phys. Rev. Lett.* **124**, 166602 (2020).
11. Nabei, Y. et al. Current-induced bulk magnetization of a chiral crystal $CrNb_3S_6$. *Appl. Phys. Lett.* **117**, 052408 (2020).
12. Shiota, K. et al. Chirality-induced spin polarization over macroscopic distances in chiral disilicide crystals. *Phys. Rev. Lett.* **127**, 126602 (2021).
13. Buongiorno Nardelli, M. et al. PAOFLOW: a utility to construct and operate on ab initio Hamiltonians from the projections of electronic wavefunctions on atomic orbital bases, including characterization of topological materials. *Comput. Mater. Sci.* **143**, 462–472 (2018).
14. Cerasoli, F. T. et al. Advanced modeling of materials with PAOFLOW 2.0: New features and software design. *Comput. Mater. Sci.* **200**, 110828 (2021).
15. Ganichev, S., Trushin, M. & Schliemann, J. Spin polarisation by current. Preprint at arXiv https://arxiv.org/abs/1606.02043 (2016).
16. Ivchenko, E. & Pikus, G. New photogalvanic effect in gyrotropic crystals. *JETP Lett.* **27**, 640 (1978).
17. Aronov, A. G. & Lyanda-Geller, Y. B. Nuclear electric resonance and orientation of carrier spins by an electric field. *Sov. Phys. JETP* **50**, 431 (1989).
18. Aronov, A., Lyanda-Geller, Y. B., Pikus, G. E. & Parsons, D. Spin polarization of electrons by an electric current. *Sov. Phys. JETP* **73**, 537–541 (1991).
19. Johansson, A., Gobel, B., Henk, J., Bibes, M. & Mertig, I. Spin and orbital Edelstein effects in a two-dimensional electron gas: theory and application to $SrTiO_3$ interfaces. *Phys. Rev. Res.* **3**, 013275 (2021).
20. Johansson, A., Henk, J. & Mertig, I. Theoretical aspects of the Edelstein effect for anisotropic two-dimensional electron gas and topological insulators. *Phys. Rev. B* **93**, 195440 (2016).
21. Ghiasi, T. S., Kaverzin, A. A., Blah, P. J. & van Wees, B. J. Charge-to-spin conversion by the Rashba–Edelstein effect in two-dimensional van der Waals heterostructures up to room temperature. *Nano Lett.* **19**, 5959–5966 (2019).
22. Tao, L. & Tsymbal, E. Y. Spin-orbit dependence of anisotropic current-induced spin polarization. *Phys. Rev. B* **104**, 085438 (2021).
23. Ziman, J. M. *Principles of the Theory of Solids* (Cambridge University Press, 1972).
24. Agapito, L. A., Ferretti, A., Calzolari, A., Curtarolo, S. & Buongiorno Nardelli, M. Effective and accurate representation of extended Bloch states on finite Hilbert spaces. *Phys. Rev. B* **88**, 165127 (2013).
25. Géranton, G. et al. Spin-orbit torques and spin accumulation in FePt/Pt and Co/Cu thin films from first principles: the role of impurities. *Phys. Rev. B* **93**, 224420 (2016).
26. Salemi, L., Berritta, M. & Oppeneer, P. M. Quantitative comparison of electrically induced spin and orbital polarizations in heavy-metal/3*d*-metal bilayers. *Phys. Rev. Mater.* **5**, 074407 (2021).

27. Doi, T., Nakao, K. & Kamimura, H. The valence band structure of tellurium. I. The *k·p* perturbation method. *J. Phys. Soc. Jpn.* **28**, 36–43 (1970).
28. Shalygin, V. A., Sofronov, A. N., Vorob'ev, L. E. & Farbshtein, I. I. Current-induced spin polarization of holes in tellurium. *J. Solid State Phys.* **54**, 2362–2373 (2012).
29. Agapito, L. A., Kioussis, N., Goddard, W. A. & Ong, N. P. Novel family of chiral-based topological insulators: elemental tellurium under strain. *Phys. Rev. Lett.* **110**, 176401 (2013).
30. Tsirkin, S. S., Puente, P. A. & Souza, I. Gyrotropic effects in trigonal tellurium studied from first principles. *Phys. Rev. B* **97**, 035158 (2018).
31. Hirayama, M., Okugawa, R., Ishibashi, S., Murakami, S. & Miyake, T. Weyl node and spin texture in trigonal tellurium and selenium. *Phys. Rev. Lett.* **114**, 206401 (2015).
32. Nakayama, K. et al. Band splitting and Weyl nodes in trigonal tellurium studied by angle-resolved photoemission spectroscopy and density functional theory. *Phys. Rev. B* **95**, 125204 (2017).
33. Anzin, V. B., Eremets, M. I., Kosichkin, Y. V., Nadezhdinskii, A. I. & Shirokov, A. M. Measurement of the energy gap in tellurium under pressure. *Phys. Status Solidi A* **42**, 385–390 (1977).
34. Tsirkin, S. S., Souza, I. & Vanderbilt, D. Composite Weyl nodes stabilized by screw symmetry with and without time-reversal invariance. *Phys. Rev. B* **96**, 045102 (2017).
35. Gatti, G. et al. Radial spin texture of the Weyl fermions in chiral tellurium. *Phys. Rev. Lett.* **125**, 216402 (2020).
36. Sakano, M. et al. Radial spin texture in elemental tellurium with chiral crystal structure. *Phys. Rev. Lett.* **124**, 136404 (2020).
37. Wimmer, S., Seemann, M., Chadova, K., Koedderitzsch, D. & Ebert, H. Spin–orbit-induced longitudinal spin-polarized currents in nonmagnetic solids. *Phys. Rev. B* **92**, 041101 (2015).
38. Seemann, M., Ködderitzsch, D., Wimmer, S. & Ebert, H. Symmetry-imposed shape of linear response tensors. *Phys. Rev. B* **92**, 155138 (2015).
39. Roy, A., Guimarães, M. H. D. & Sławińska, J. Unconventional spin Hall effects in nonmagnetic solids. *Phys. Rev. Mater.* **6**, 045004 (2022).
40. Zhang, N. et al. Magnetotransport signatures of Weyl physics and discrete scale invariance in the elemental semiconductor tellurium. *Proc. Natl Acad. Sci. USA* **117**, 11337–11343 (2020).
41. Ideue, T. et al. Pressure-induced topological phase transition in noncentrosymmetric elemental tellurium. *Proc. Natl Acad. Sci. USA* **116**, 25530–25534 (2019).
42. Onuki, Y. et al. Chiral-structure-driven split fermi surface properties in $TaSi_2$, $NbSi_2$, and VSi_2. *J. Phys. Soc. Jpn.* **83**, 061018 (2014).
43. Zhu, H., Yang, T., Zhou, Y., Hua, S. & Yang, J. Theoretical prediction on the structural, electronic, mechanical, and thermodynamic properties of $TaSi_2$ with a C_{40} structure under pressure. *Z. Naturforsch. A* **74**, 353–361 (2019).
44. Garcia, C. A. C., Nenno, D. M., Varnavides, G. & Narang, P. Anisotropic phonon-mediated electronic transport in chiral Weyl semimetals. *Phys. Rev. Mater.* **5**, L091202 (2021).
45. Acosta, C. M., Yuan, L., Dalpian, G. M. & Zunger, A. Different shapes of spin textures as a journey through the Brillouin zone. *Phys. Rev. B* **104**, 104408 (2021).
46. Aroyo, M. I. et al. Bilbao crystallographic server: I. Databases and crystallographic computing programs. *Z. Kristallogra.—Cryst. Mater.* **221**, 15–27 (2006).
47. Aroyo, M. I., Kirov, A., Capillas, C., Perez-Mato, J. M. & Wondratschek, H. Bilbao Crystallographic Server: II. Representations of crystallographic point groups and space groups. *Acta Crystallogr. A* **62**, 115–128 (2006).
48. Chang, G. et al. Topological quantum properties of chiral crystals. *Nat. Mater.* **17**, 978–985 (2018).
49. Bernevig, B. A., Orenstein, J. & Zhang, S.-C. Exact SU(2) symmetry and persistent spin helix in a spin–orbit coupled system. *Phys. Rev. Lett.* **97**, 236601 (2006).
50. Giannozzi, P. et al. QUANTUM ESPRESSO: a modular and open-source software project for quantum simulations of materials. *J. Phys. Condens. Matter* **21**, 395502 (2009).
51. Giannozzi, P. et al. Advanced capabilities for materials modelling with QUANTUM ESPRESSO. *J. Phys. Condens. Matter* **29**, 465901–31 (2017).
52. Corso, A. D. Pseudopotentials periodic table: from H to Pu. *Comput. Mater. Sci.* **95**, 337–350 (2014).
53. Perdew, J. P., Burke, K. & Ernzerhof, M. Generalized gradient approximation made simple. *Phys. Rev. Lett.* **77**, 3865–3868 (1996).
54. Agapito, L. A., Curtarolo, S. & Buongiorno Nardelli, M. Reformulation of DFT+U as a pseudohybrid Hubbard density functional for accelerated materials discovery. *Phys. Rev. X* **5**, 011006 (2015).
55. Agapito, L. A., Ismail-Beigi, S., Curtarolo, S., Fornari, M. & Buongiorno Nardelli, M. Accurate tight-binding Hamiltonian matrices from ab initio calculations: minimal basis sets. *Phys. Rev. B* **93**, 035104 (2016).
56. Agapito, L. A. et al. Accurate tight-binding Hamiltonians for two-dimensional and layered materials. *Phys. Rev. B* **93**, 125137 (2016).
57. Kawamura, M. FermiSurfer: Fermi-surface viewer providing multiple representation schemes. *Comput. Phys. Commun.* **239**, 197–203 (2019).
58. Koralek, J. D. et al. Emergence of the persistent spin helix in semiconductor quantum wells. *Nature* **458**, 610–613 (2009).

ACKNOWLEDGEMENTS

We are grateful to Bart van Wees, Xu Yang, and Caspar van der Wal for the insightful discussions that inspired us to initiate this project. J.S. acknowledges the Rosalind Franklin Fellowship from the University of Groningen. The calculations were carried out on the Dutch national e-infrastructure with the support of SURF Cooperative (EINF-2070), on the Peregrine high-performance computing cluster of the University of Groningen and in the Texas Advanced Computing Center at the University of Texas, Austin.

AUTHOR CONTRIBUTIONS

J.S., A.R., and K.T. performed the DFT calculations. A.R. conceived and analyzed model Hamiltonians. J.S., F.C., M.B.N, A.R., and A.J. implemented the method. A.R. and J.S. compiled the figures and wrote the manuscript. J.S. proposed and supervised the project. All authors contributed to the analysis and discussion of the results.

COMPETING INTERESTS

The authors declare no competing interests.

ADDITIONAL INFORMATION

Correspondence and requests for materials should be addressed to Jagoda Sławińska.

Reprints and permission information is available at http://www.nature.com/reprints

Publisher's note Springer Nature remains neutral with regard to jurisdictional claims in published maps and institutional affiliations.